Uptake and Diffusion of Ions in Organically Synthesized Porous Carbon for Battery Anode Applications

P. Heasman, A. Trewin*

Lancaster University, Lancaster, LA1 4YB, UK

Abstract: Organically synthesized porous carbon (OSPC-1) has a high lithium uptake of 748 mAh g^{-1} demonstrating that it is a strong contender as an anode material for lithium ion batteries (LIBs). Simulations of the lithium uptake on models generated of OSPC-1 gave values close to the experimentally obtained data. Thus we assess the potential of OSPC-1 for use as an anode material in batteries of sodium, potassium, magnesium, and calcium. We find ion uptakes of 770, 386, 158, and 774 mAh g^{-1} for Li^+, Na^+, K^+, and Ca^{2+}, respectively. We also study the diffusive capabilities of ions through the OSPC-1 structure via means of *active diffusion*. The lithium ions were able to diffuse at a greater rate, followed by the divalent ions, Mg^{2+} and Ca^{2+}, and the monovalent ion, Na^+ and K^+. All of the ions were able to diffuse completely through the OSPC-1 structure with the diffusion rate being dependent on the ionic radius of the ion, coupled with the valency of the ion. Therefore we show that OSPC-1 also has great potential as an anode material for Na^+, K^+, Mg^{2+}, and Ca^{2+} batteries.

1. Introduction

Carbon is a very useful element as it has many biological and technological applications. Alongside its naturally occurring forms of diamond and graphite, synthetic allotropes include nanotubes, graphene, and graphite. The first allotropes synthetically developed were fullerenes by Kroto et al.[1] This has led to the development of a vast array of carbon allotropes with varying sp^2- and sp^3- hybridization.

Graphite is the most widely used commercial anode in lithium ion batteries. However, graphite swells upon lithium ion uptake, and thus results in fractures and destruction of the crystal structure. Also, the formation of lithium dendrites on the graphite-electrolyte interface can cause the battery to short circuit. In addition, graphite has a low theoretical capacity (350mAh g^{-1}). There is therefore a need for alternative carbon-based materials to act as alternative anodes materials for battery technologies.[2,3] Alternative anode materials include metal-oxide anodes,[4–6] layered sheets,[7] micro and nano constructs,[7] porous nanocages,[8] metal-oxide porous nanosheets,[9] and metal-organic frameworks.[10]

OSPC-1 (organically synthesized porous carbon) (SA_{BET} = 766 m^2 g^{-1}), has electron conductivity, an ability to be charged with more than twice the amount of lithium as compared to the graphite electrodes in state-of-the-art lithium ion batteries (LIBs), and an ability to be charged at a high rate without any signs of detrimental lithium plating or dendrites that can cause explosions of devices. Thus OSPC-1 is a strong contender as a future anode material in lithium ion batteries.[11]

OSPC-1 is synthesized via a catalytic Eglinton homo-coupling[12] of ethynyl methane (Figure SI.1) The PXRD pattern shows an amorphous structure, as no Bragg diffraction peaks are observed. A BET surface area of (SA_{BET}) 766 m^2g^{-1} was determined via analysis of the nitrogen uptake isotherm. Conductivity measurements show a conductivity of 1.2 x10^{-4} S cm⁻

[1], making OSPC-1 a semiconducting carbon material. This is attributed to a quantum tunneling effects between the *sp-* orbitals of adjacent struts of the same node.

A reversible lithium ion uptake of 748 mAh g^{-1} is obtained at a current density of 200 mA g^{-1} over 100 cycles. This exceeds many alternative carbon materials, including C_{60} (2.5 mAh g^{-1}), carbon nanotubes (324 mAh $^{-1}$), and graphite (324 mAh g^{-1}). There is reversible capacity at higher current densities. More notably, upon reducing the current density back to 100 mA g^{-1}, a very similar capacity is obtained to the initial cycle, offering a rate capacity of 944 mAh g^{-1}. The long cycle life and high capacity demonstrate the stability of the interactions with lithium ions, along with its open framework, giving rise to a large internal storage space.

Trewin *et al.* produced OSPC-1 models through the in-house code AmBuild[14] and were able to simulate the lithium-ion capacity through simulated annealing using the *Sorption* module in Materials Studio,[13] giving a theoretical capacity of lithium ion uptake which equated to 420-579 mAh g^{-1} as calculated using Faraday's Law. These models reflect the microporous properties of the OSPC-1 structure, and do not take into account the mesoporous regions of the material. It was postulated that the mesopore region may contribute to the total uptake. Based upon the ratio of volume within the microporous and mesoporous areas obtained through the nitrogen uptake isotherm, a total capacity of 786 mAh g^{-1} is obtained, in high agreement with the experimental value of 748 mAh g^{-1}.

Molecular Dynamics (MD) simulations of lithium ion activated diffusion highlighted the diffusion pathway through the OSPC-1 pore system. A simulation cell was generated using AmBuild with the OSPC-1 polymer grown between two graphene sheets. Lithium ions were seeded at the top of the simulation cell and charge applied to the graphene sheets so that the charge bias results in diffusion of the Li ions from the top of the simulation cell next to the positively charged graphene sheet, to the bottom of the cell where the negatively charged graphene sheet is located. We have termed this as *active diffusion*.

Due to its excellent performance as an anode for lithium-ion batteries, it is interesting to establish how OSPC-1 behaves for alternative ions. The development of new battery materials is key for technology progression. Due to the growing portable device industry, lithium ion batteries are becoming of high demand, with lithium ion supplies depleting at a fast rate. As alternatives to lithium ion batteries, batteries of sodium,[14,15] potassium,[14,16] calcium,[17–19] and magnesium[20] have been studied.

Sodium ion batteries (SIBs) have been a concept for many years. Early studies showed how sodium ions (Na^+) could be incorporated into carbon structures such as graphite, offering capacities from 30 mA h g^{-1} to 140 mA h g^{-1}.[21] Recent studies have shown the development of graphene-based, and many carbon-based anode materials for sodium ion batteries.[22–24] Several nitrogen-doped materials have shown charge capacities of up to 1000 mA h g^{-1} with a current density of 0.1 A g^{-1}.[25] Porous materials have also been studied for their potential as sodium-ion batteries. Ji et al. displayed the charge capacity capabilities of porous carbon frameworks.[26] This porous material displayed a charge capacity of 290 mA h g^{-1} with a current density of 0.2 A g^{-1}. Similarly, a mesoporous soft carbon material has shown great recyclability over 3000 cycles (103 mA h g^{-1} at 0.5 A g^{-1}). The maximum charge capacity of this material exceeded that of the porous carbon framework with 331 mA h g^{-1} at 0.03 A g^{-1} charge density.[27]

Potassium-ion batteries (KIBs) have received much interest recently due to the availability and affordability of resources. Recent advancements have seen the development of 3-dimensional carbon frameworks as anode materials for potassium ion batteries.[28] KIBs based on a perylene-tetracarboxylic acid-dianhydride (PTCDA) cathode[29] and dipotassium terephthalate (K_2TP)[30] anode have shown great promise towards stable cycling performance. PTCDA based KIBs showed a specific capacity of 131 mA h g^{-1} with a potential range of 1.5-3.5 V vs. K/K^+, and retained a stable cycling performance over 200 cycles. This

particular material demonstrated a great increase in capacity with a potential of 0.01 V vs. K/K$^+$ (753 mA h g^{-1}). The K$_2$TP anode demonstrated a high capacity retention of 94.6 % over 500 cycles, and a specific capacity of 249 mA h g^{-1}. Jiang et al. have introduced several conjugated microporous polymer (CMP) materials that include benzothiadiazole.[31] These materials exhibit great band gap changes from changing the phenyl linker to benzothiadiazole.[32] However, there is a movement of electron density by incorporation of benzothiadiazole, allowing K$^+$ to readily interact with the electron rich sites. This results in a capacity of 428 mA h g^{-1}.

The capacities of these materials as KIBs are still comparably smaller to LIBs, although potassium ions possess larger ionic radii to both lithium and sodium ions. A large volume change commonly ensues from the size of potassium ions resulting in poor cyclability in comparison to lithium ion batteries.

Magnesium ion battery technology (MIBs) is still young in comparison to LIBs. Magnesium is a suitable choice as an ion due to its much lower price and toxicity. In comparison to lithium, magnesium provides a considerably high volumetric energy density alongside its high volumetric capacity (2200 mA h g^{-1} 3800 mA h cm^{-3}).[33] However, the main difficulties of developing MIBs has been the electrolyte solution, as proton donating nor accepting show to be unsuitable, and also the choice of cathode material, as magnesium is not easily intercalated into many hosts.[34,35] Aurbach et al. first introduced a rechargeable MIB with a capacity of 122 mA h g^{-1}.[36] Since then, research has focused on developing materials that approach the challenges MIBs face. Doi et al. showed the capabilities of potential positive electrodes for MIBs, demonstrating their high electrical conductance.[37] More recent advances have seen the development of rechargeable MIBs displaying rate capabilities up to 200 mA h g^{-1}.[38,39]

Calcium ions show great potential within the field of battery technologies.[27] However, additional research is required for them to reach their full potential, and to demonstrate properties that lithium-ion batteries have displayed. Development of calcium-ion batteries (CIBs) has faced several challenges, one including the lack of redox processes at room temperature, although the greater abundance of calcium available compared to lithium proves to be a beneficial factor towards CIB progression.[18,40]

2. Methods

Here we assess the capacity and the activated diffusion pathways of lithium ions in more detail and compare to the diffusion and uptake of these alternative ions. A set of four OSPC-1 models were generated using the AmBuild code, as described previously with the building block given in Figure SI.2, with a cell size of 50 x 50 x 50 Å. The resulting models are shown in SI.3 with a comparison of their structural properties to measured experimental data (Table SI.1). The maximum uptake of each ion was calculated for two 25 x 25 x 25 Å samples of each cell using the *Sorption* module of Materials Studio, which utilizes a simulated annealing approach giving a total of eight uptake values for each ion. For lithium, sodium, potassium, and calcium the PCFF[41] force field was used. The PCFF force field were chosen to best replicate the experimental uptake, see SI Section 3 for further discussion and a comparison of the values calculated for other force fields. The capacity is calculated using Faraday's Law (Figure SI.6) using the maximum uptake of each ion determined.

For the active diffusion simulations, the OSPC-1 structure was generated within two slabs of graphene, shown in Figure SI.4 and Figure SI.5, with the graphene slabs at $z= 2$ Å and $z= 68$ Å charged positively and negatively respectively. Fifteen lithium ions were seeded randomly between $z= 66$ Å and $z = 63$ Å, adjacent to the positively charged graphene slab, shown in Figure SI.5. Molecular dynamic simulations were ran using the NVT ensemble, the Hoover thermostat, with a temperature of 0 K, using the DL Poly molecular dynamic code.

After 2000 steps the carbon atoms in each graphene sheet were charged positively and negatively with each carbon atom having +/-1 charge respectively. The active diffusion of the lithium ions through the OSPC-1 system was monitored, along with any structural changes. The lithium ions in their original positions were directly replaced with sodium, potassium, magnesium, and calcium ions so that the diffusion pathway of each ion can be directly compared. For the OSPC-1 structure, graphene, lithium, sodium, potassium, and calcium the PCFF[19] parameters were used, however the parameters from the COMPASS force field[29] were used for magnesium.

3. Results and Discussion

3. 1 Capacity

Figure 1a shows an example of the uptake of each ion in the same OSPC-1 sample and Table 1 shows the average value for the capacity of each ion across the eight OSPC-1 structure samples. Table SI. 2-5 shows all the uptake values and the corresponding calculated capacity.

The highest calculated capacity was for calcium, followed closely by lithium with 774 mAh g^{-1} and 770 mAh g^{-1} respectively. Sodium gives a calculated capacity of 386 mAh g^{-1}. The lowest calculated capacity is for potassium at 158 mAh g^{-1}. Figure 1b shows the capacity for each ion plotted against the radius of the respective ion. The group 1 ions are shown in orange with a clear decreasing trend as you move down the group. This is most likely due to the increasing radius limiting the number of ions that can be taken up by the OSPC-1 structure due to the size of the pores available. Sodium and calcium have very similar ionic radius and so a direct comparison can be made. For each sample, a very similar number of sodium and calcium ions are absorbed into the pore structure. The calculated capacity of calcium ions is double that of sodium simply due to the divalent charge of the calcium ion

whereas the sodium is monovalent. Calcium therefore fits the trend of decreasing uptake due to the increasing radius of the ions.

The calculated capacities show that there is great potential for the OSPC-1 material to have excellent capacity when used as an anode for other ion batteries. In particular, the OSPC-1 material seems to have a high predicted capacity for calcium which, coupled with its relative abundance, makes this a system of particular interest.

3.2 Lithium Ion Diffusion

Each lithium ion in the simulation cell was readily able to diffuse through the OSPC-1 structures generated. The first lithium ion was able to establish a direct pathway through the structure with little sign of blockage of the pathway through the OSPC-1 structure. Figure 2 and Figure SI.8 illustrates the diffusion pathway and the z-axis movement of Li1 during the MD simulation. Initially, the lithium ion moves slowly, due to Li1 moving around the first carbon atom before it is able to determine its pathway. Once the lithium ion has maneuvered around the carbon framework, its movement in the z-axis was fast, taking approximately 1000 steps to diffuse through to the negatively charged graphene sheet.

The additional lithium ions demonstrate very similar diffusive behavior through the OSPC-1 structures generated. Each ion is able to completely diffuse through the structure towards the negatively charged graphene sheet. Figure SI. 9 illustrates the z-axis movement for the lithium ions Li2 to Li15. Each ion goes through the same establishment procedure as Li1, showing slow movement at first when the charge is applied, followed by faster diffusion once a pathway is found. They are able to move approximately 10 Å from their origin, but there is then reduced movement for several hundred steps. The ions are then able to establish a new pathway that is highly direct, giving it a very short transport time from this point; for example, Li4 shows a very direct pathway to the negatively charge graphene once a pathway is established. Several ions highlight areas of the OSPC-1 that are densely packed where the

lithium ions become trapped in pockets or 'dead-ends' in the pore network. The active diffusion rates for the lithium ions in OSPC-1 are shown in Table SI.6 and are calculated from step 2000 of the simulation. The rate at which the lithium ions diffused is greatly affected by these dead-ends, although, as shown with the diffusion simulation, these lithium ions were eventually able to completely diffuse through the OSPC-1 structure generated.

Due to these diffusion rates being calculated from the active diffusion, they are larger than the charge-free experimental diffusion coefficients ($\sim$4 x10^{-4} cm^2 s^{-1}). Therefore, the rates are used to demonstrate the available pathways within OSPC-1, and also how the structure can affect the movement of lithium ions through its confines. Figure SI.10 illustrates further how each lithium ion differs in diffusion rate, and how each differs to the average rate calculated from the simulation.

To determine how the carbon framework is affected by the movement of the lithium ions, and vice versa, the distance between the fastest moving and slowest moving lithium ions (Li12 with an active diffusion rate of 5.94 x10^4 cm^2 s^{-1}; Li4 with an active diffusion rate of 3.32 x10^4 cm^2 s^{-1}) and the nearest carbon atoms were measured (Figure SI.11). The distance of the closest carbon was determined for every 50 steps of the simulation. Both ions show fluctuations in distance as they travel through the system, yet the faster ion (Li 12) displays a greater distance throughout its diffusion. Li12 has a wider pathway (average = 2.486 Å), whereas Li4 has a much narrower pathway (average = 2.364 Å), and therefore a more difficult path for the lithium ion to traverse. With the diameter of the lithium ion being 2.8 Å, Li4 is less able to move through along the narrower pathway and was only able to force its way through at approximately step 3750. The actively diffusing ions force the OSPC-1 structure to move and therefore allow the lithium ion to pass. This is shown in Figure SI. 13. The distance between these specific carbon atoms of OSPC-1 increase as the lithium ion

passes between them, proving how the flexibility of the node-to-node struts allows the carbon structure to shape around the lithium ions as they pass through the system.

Several carbon-carbon distances were observed during the lithium ion diffusion simulation. Figure SI. 15 shows these separations over the simulation period. The structure of OSPC-1 contains available channels for the lithium ions to travel, however, there are pathways in which several ions travel that are narrower than the available channel. The sp^3-sp^3 struts bend and flex to allow the passage of ions through the system. The flexibility of the OSPC-1 structure allows the lithium ions to establish a more open volume within the material, therefore allowing the lithium ions to readily diffuse through the system. The charge bias in influences the movement of the carbon atoms of OSPC-1 as the lithium ions are being force in one direction. Table SI.7 shows the distance between the carbon atoms observed.

This movement shows that the pathways available within the OSPC-1 structure are still not wide enough to allow lithium ions to pass through. The active diffusion of the simulation forces the lithium ions through the system, which in turn moves the carbon atoms within the OSPC-1 structure to allow passage. The average movement of the carbon atoms is 1.162 Å.

3.3 Sodium-ion Diffusion

Sodium ions possess an ionic radius larger than that of lithium (Na, 1.16 Å; Li, 0.9 Å). All of the 15 sodium ions observed in this simulation were able to completely diffuse through OSPC-1 towards the negatively charged graphene sheet. This shows that the OSPC-1 structure generated is capable of allowing ions with larger ionic radius to pass through its structure.

Na1 was able to diffuse completely through the OSPC-1 structure and the diffusion pathway of Na1 is shown in Figure SI.16. Na1 established a pathway that allowed it to diffuse completely through the OSPC-1 structure with ease. The movement in the z-axis showed little to no reduction in the rate of movement, Figure SI. 17.

Many of the pathways established by the sodium ions observe little obstruction and reduced movement due to OSPC-1. However, Na3 and Na4 encounter areas of the structure generated to which they were required to establish an alternate route to diffuse through, resulting in a reduction in diffusion rate. Both Na3 and Na4 had slower diffusion rates to the additional sodium ions (Table SI.8) with Na4 displaying the slowest diffusion rate of 2.37 $x10^4$ cm s^{-1}.

The diffusion rate of the sodium ions is much slower in comparison to the lithium ion diffusion. The average diffusion rate of the lithium ions was 4.78 $x10^4$ cm s^{-1}, whereas the average sodium ion diffusion rate was 3.30 $x10^4$ cm s^{-1}. The ions of larger ionic radius diffuse more slowly, as the sodium ions must establish wider pathways to diffuse through. As the respective ions have the same starting position, the comparable diffusion rates are therefore dependent on the size of the ion and the pathway established by each ion in the simulation. Comparing the diffusion pathways of Na1 and Li1 (Figure 3 and Figure SI.19), we can see that they were able to establish almost identical pathways through OSPC-1. However, the size of the sodium ion results in it moving at a slower rate through the structure than that of the lithium ion. Both ions encounter an obstruction at 45 Å, where the sodium ion appeared to have no movement between 2000 and 2500 steps, and the lithium ion showed reduced movement. After 2500 steps the lithium ion was able to move rapidly. At 2770 steps we could see the difference in position between the two different ions as they traversed the system. Figure SI.20 displays the positions of both Na1 and Li1 at step 2770.

This demonstrates that ionic radius is also a determining factor for ion diffusion through OSPC-1, alongside the construction and formation of the porous network. Figure SI.18 illustrates the difference in calculated diffusion rates between the sodium ions and lithium ions through OSPC-1.

Although the diffusion rate is slower for the sodium ions in comparison to the lithium ions observed, a complete diffusion was possible for the sodium ions through OSPC-1. The pathways determined for each sodium ion do not differ greatly from those established by the lithium ions. This shows that OSPC-1 has a potential as an anode for sodium ion batteries, offering pathways for the sodium ions to diffuse through. However, the ions encountered more obstructions and had a slower diffusion rate due to their ionic radius.

3.4 Potassium-ion Diffusion

The lithium ions were replaced with potassium ions for the active diffusion simulation. Similar to the lithium ions and sodium ions, each potassium ion was able to diffuse completely through the structure generated to the negatively charged graphene sheet. K1 (Figure SI.21) was able to establish a diffusion pathway similar to that of Na1 and Li1.

However, in comparison to the calculated diffuse rates and movement in the z-axis, K1 diffused more slowly than Li1 and Na1 through OSPC-1. The potassium ion showed a further reduction in movement for the first several hundred steps post charge application, followed by a further reduction in movement through the construct. Figure SI.22 shows the movement of K1 in the z-axis. The potassium ion diffused over approximately 2000 steps, whereas Li1 and Na1 diffused to the negatively charged graphene sheet after 1200 and 1800 steps, respectively. The increased size of the potassium ions resulted in slower diffusion rates and reduced movement through OSPC-1. However, the porous construct of OSPC-1 posed no challenge for the potassium ions to pass through, with each ion diffusing completely. Although each ion was able to diffuse completely through OSPC-1, several ions showed periods of reduced movement where they were required to navigated blockages or narrower channels.

K4 is an example of a potassium ion encountering a blockage along its pathway shown in Figure SI. 23. Li4 also encounters this obstruction, although the duration in which the

potassium ion took to overcome the blockage and continue on its diffusion pathway is greater than that of the lithium ion. Li4 becomes blocked for approximately 500 steps, whereas K4 takes over 1000 steps to establish an alternate route. The comparison between the z-axis movement of K4 and Li4 is shown in Figure 3. Li4 diffuse at a greater rate before becoming trapped, and then continued to diffuse at a great rate once released. K4, on the other hand, diffused at a slower rated to begin with, but displayed a greater rate of diffusion once it had navigated the blockage.

As well as becoming trapped for a longer duration than Li4, K4 was required to establish a different route to that of Li4 (Figure SI.23). The potassium ion can be seen following a similar pathway to Li4 before the blockage, and then diverts onto a differing path to complete its diffusion. The potassium ion was unable to follow the lithium ion along the same pathway due to its larger ionic radius, and the size of the pathway.

The diffusion rates calculated for the potassium ions did not surpass the diffusion rates of any of the lithium ions (Table SI.9).The average diffusion rate for of the potassium ions was calculated at 2.64 $\times 10^4$ cm s^{-1}, whereas the average diffusion rate for the lithium ions was 4.78 $\times 10^4$ cm s^{-1}. Comparably, the average diffusion rate of the sodium ion diffusion was calculated to be 3.30 $\times 10^4$ cm s^{-1}. This study of group 1 ions diffusing through OSPC-1 demonstrates that the ionic radius of the ions is a highly impacting factor on their diffusion. The average diffusion rate decreases going down the group from lithium ions to potassium ions.

The comparison between the individual lithium ions and potassium ions through OSPC-1 is shown in Figure SI.24. As previously observed, K4 becomes trapped within the OSPC-1 structure, forcing the ion to establish a new direction. Because of this obstruction, K4 was the slowest potassium ion to diffuse through (1.88 $\times 10^4$ cm s^{-1}), whereas K15 was the fastest to diffuse through, at 3.13 $\times 10^4$ cm s^{-1}. The diffusion rate of K15 was much slower in

comparison to both Li15 and Na15 (5.73 $x10^4$ and 3.30 $x10^4$ cm s^{-1}, respectively), demonstrating how the size of pores within the microporous structure, as well as the size of ionic radius, affect the transport of ions.

This study showed that OSPC-1 has the capacity to allow potassium ion diffusion through its structure, and therefore a potential candidate as an anode for KIBs. However, the larger ionic radius of the potassium ions resulted in a slower diffusion rate. Additionally, the pathways available for the lithium ions were not as readily accessible for the potassium ions (as seen with Li4 and K4), which presented obstructions and blockage to which the potassium ions were required to deviate from the lithium ion pathway.

3.5 Magnesium-ion Diffusion

Each of the magnesium ions in the simulation were able to diffuse completely through OSPC-1 to the negatively charged graphene sheet, establishing diffusion pathways that presented minor obstructions as they traverse the system. Figure SI. 25 shows the diffusion pathway of Mg1 through OSPC-1. Mg1 was able to establish a direct pathway through OSPC-1 with no obvious blockages (Figure SI. 26). The magnesium ion encountered a similar obstacle to that of Li1 at the beginning of its diffusion, having started to follow the same pathway as that of the lithium ion. However, Mg1 diverted from that pathway and established a different route, in which it encountered very few obstacles as it traversed the system, resulting in a final position that was different to that of the lithium ion at the negatively charged graphene.

Despite the ionic radius of the magnesium ions being similar to that of the lithium ions, the diffusion pathway of Mg1 greatly differed. An example of the magnesium ions establishing a different diffusion pathway to their respective lithium ions is Mg3. The magnesium ion diverts from the lithium ions pathway within the early stages of the simulation. However, both ions converge to a very similar position at the negatively charged graphene sheet (Figure

SI. 27). The diffusion pathway established for Li3 appears to be more contorted compared to that of Mg3. However, the chosen diffusion pathway for Mg3 contained more obstructions. This was apparent from their diffusion rates and movement through the z-axis (Figure 3). Mg3 showed a reduction in movement at approximately 55 Å but was able to continue its diffusion without further obstruction. The rate at which it diffused after overcoming the obstacle was still slower than that of Li3, resulting in the ion diffusing over 2000 steps, whereas Li3 took 3500 steps. This was similar for the additional magnesium ions. The majority of magnesium ions established direct pathways through OSPC-1, although, such examples as Mg3, Mg9, and Mg11 encountered more obstructions during their diffusion. With the exception of Mg4 and Mg6, the diffusion rates calculated for each magnesium ion was slower than their respective lithium ions. The individual calculated diffusion rates of the magnesium ions are shown in Table SI.10.

Due to obstruction in the pathway, Mg3 presented the slowest diffusion rate of all the magnesium ions with 3.09×10^4 cm s^{-1}, whereas Mg13 showed the fastest diffusion rate of the series with 4.79×10^4 cm s^{-1}. In comparison to the lithium ions, the average diffusion rate is slower. The lithium ions presented an average diffusion rate of 4.87×10^4 cm s^{-1}, compared to 3.94×10^4 cm s^{-1} of the magnesium ions (Figure SI.28).

The maximum diffusion rate observed of the magnesium ions did not surpass the average diffusion rate calculated of the lithium ions through OSPC-1. However, the magnesium ion diffusion rates were greater than those calculated of the sodium ions and potassium ions 3.30×10^4 and 2.64×10^4 cm s^{-1}, respectively). This was due to the ionic radius of magnesium being smaller than both sodium and potassium, resulting in a greater diffusion rate than both of the group 1 ions. Additionally, magnesium holds a 2+ charge, which is more strongly attracted to the negatively charged graphene sheet than the group 1 ions, allowing it to move through OSPC-1 and force any bond movement of the carbon structure.

3.6 Calcium-ion Diffusion

Ca1 (Figure SI.29) was able to diffuse completely through OSPC-1 towards the negatively charged graphene sheet. The pathway resembles that established by Mg1, finishing in a very similar position. Calcium has a much larger ionic radius out of the two divalent ions observed. However, each individual ion was able to establish a full pathway through the OSPC-1 structure. The divalent ions are more strongly attracted to the negatively charged graphene sheet, which has potential to force greater movement in the OSPC-1 structure. However, the size of these ions inhibits their trajectory, as previously seen with the larger of the group 1 ions.

The pathways established by Li1 and Ca1 are almost identical for the first 35 Å through OSPC-1. At this point the calcium ion deviates from the pathway taken by Li1 and is able to establish an alternate pathway to complete its diffusion to the negatively charged graphene sheet. The calcium ion was able to force the movement of the OSPC-1 framework, allowing it to diffuse along its desired pathway, whereas the lithium ion becomes trapped. As the calcium ion possess a stronger attraction and repulsion to the charged graphene sheets, it is able to force its way through. The lithium ion, on the other hand, becomes trapped for approximately 200 steps, shown in Figure SI.30. As shown in Figure 3, the Ca6 moves steadily through the structure once the charge is applied. Whereas Li6 moves in a step-like fashion, displaying fast diffusion before encountering blockages at several regions along its diffusion pathway. Both ions appear to arrive at the same positions in z-axis at within the same time period. However, due to the faster movement of the lithium ion between each blockage, overall it is able to diffuse at a greater rate than the calcium ion. The diffusion rate of Ca6 was calculated to be 2.83×10^4 cm s^{-1} (Table SI. 11), whereas Li6 displayed a diffusion rate of 3.30×10^4 cm s^{-1}. Additionally, the respective calcium ions diffused at slower

rates to the lithium ions, giving a calculate average diffusion rate of 3.06 $\times 10^4$ compared to 4.87 $\times 10^4$ cm s^{-1} from the lithium ions.

Despite having an ionic radius smaller than both of the larger monovalent ions, the diffusion rate calculated of the calcium ions did not surpass that of the sodium ions (3.30 $\times 10^4$ cm s^{-1}), which had an ionic radius slightly larger than that of Ca^{2+}. However, the calculated average diffusion rate of the calcium ions was greater than the average of the potassium ions (2.64 $\times 10^4$ cm s^{-1}). Figure SI. 31 illustrates the differences in diffusion rate between the individual lithium and calcium ions that result in the difference in average diffusion rates calculated.

3.7 Comparison

The lithium ions observed in this study showed the greatest diffusion rate through OSPC-1 in comparison to the alternative metal ions (Table 2). The smaller ionic radius allows the Li$^+$ to ions find suitable pathways to traverse, without resorting to forcing their way through the structures. Analysis of the diffusion pathways established by the ions show that OSPC-1 is capable of allowing lithium, sodium, potassium, magnesium, and calcium ions to pass through, although the ions with larger ionic radius were forced to take different pathways. This resulted in potassium displaying the slowest diffusion rate. Magnesium and calcium possess smaller ionic radii to those of sodium and potassium, allowing them to move through smaller microporous pathways. With the exception of lithium, the divalent ions have greater diffusion rates than their respective monovalent ions in each period (Mg^{2+} > Na$^+$; Ca^{2+} > K$^+$). Comparing the diffusion rates of each ion showed the correlation between the size of ionic radius the diffusive capabilities of OSPC-1 (Figure 4), both the monovalent and divalent ions decrease in diffusion rate as the ionic radius increased down the periodic group. Sodium and calcium possess very similar ionic radii, therefore give diffusion rates that are very similar at 3.28 $\times 10^4$ cm s^{-1} and 2.90 $\times 10^4$ cm s^{-1}, respectively. Magnesium ions have a much greater

diffusion rate than that of sodium, potassium, and calcium. The reduced ionic radius, alongside the +2 charge, allow them to diffuse more readily, giving rise to an average diffusion rate of 3.71 $\times 10^4$ cm s^{-1}. This can be utilized to estimate the diffusion rates of ions within the groups. For example, the plotted curve between the magnesium and calcium ion diffusion rates could be extrapolated to estimate the diffusion rates of beryllium ions and also strontium ions.

The lithium, sodium, and calcium ions disrupt the carbon framework less than magnesium and potassium. The RMSD of the carbon atoms in the OSPC-1 structure for each ion, shown in Figure 5, shows that the potassium ion induces the most movement of the OSPC-1 structure and sodium the least movement. Potassium has the largest ionic radius; it would be expected that they would enforce greater movement upon the carbon framework of OSPC-1 compared to the alternative ions (Figure 5). The carbon network was required to move to allow all of the ions to diffuse through. However, the established pathways between all of the ions differ. Because of this, the chosen pathways of the smaller ions contained more blockages, resulting in greater movement of the system.

4. Conclusion

In conclusion, the capacity of OSPC-1 with a variety of ions was calculated through uptake simulations. The value determined for lithium matched very well to the value determined experimentally. The capacity calculated from the uptake values obtained for sodium, potassium and calcium in OSPC-1 are promising for future battery systems. It is challenging to compare to capacity values determined experimentally for different systems as the charging current varies and dramatically influences the capacity values obtained. However, for graphite/Ca systems a capacity of 744 mA h g^{-1} was determined, similar to the OSPC-1/Ca value determined here.[46] For sodium a value of 270 mA h g^{-1} was determined for hard carbon/Na smaller than the capacity of 386 mA h g^{-1} determined for OSPC-1/Na.[46] All the

ions observed were able to establish pathways through the structure that allowed for complete diffusion. However, the structure was required to move to allow for the passage of ions. Both the size of the ion and their ionic charge were diffusion rate determining factors, as well as affecting the established pathway of each ion in the system. This study has shown that OSPC-1 has great potential for sodium, potassium, magnesium, and calcium ion batteries.

Supporting Information. 1. OSPC-1 synthetic procedure. 2. OSPC-1 model generation, ion uptake, ion diffusion system setup. 3. Plots for: lithium ion diffusion, sodium ion diffusion, potassium ion diffusion, magnesium ion diffusion, and calcium ion diffusion.

Corresponding Author

*A. Trewin. * a.trewin@lancaster.ac.uk

Author Contributions

The manuscript was written through contributions of all authors. All authors have given approval to the final version of the manuscript.
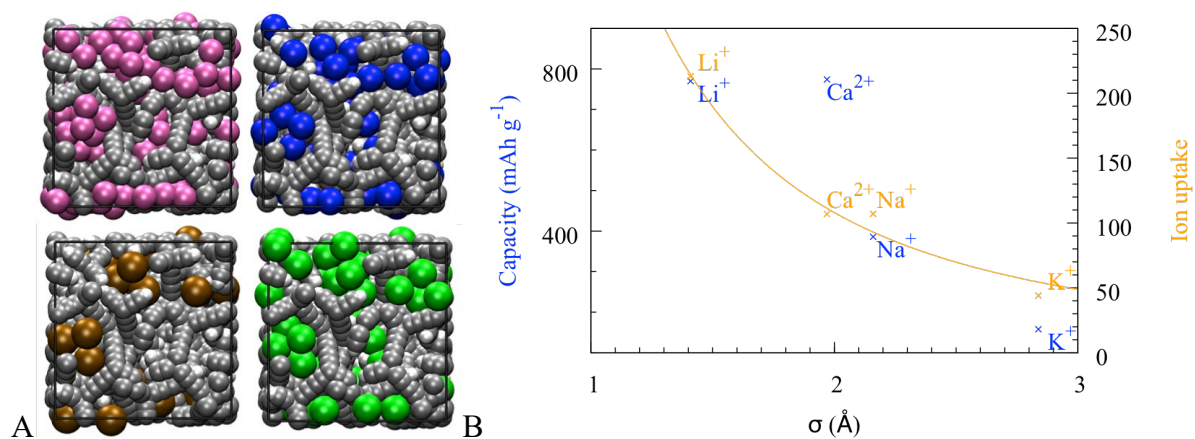
Figure 1. (a) Ion uptake in OSPC-1. Grey – carbon, white – hydrogen, pink – lithium, blue – sodium, brown – potassium, and green – calcium. (b) Plot of the average number of ions taken up by the OSPC-1 models (orange – right y axis) and the calculated capacity (blue – left y axis) against σ (ion radius).
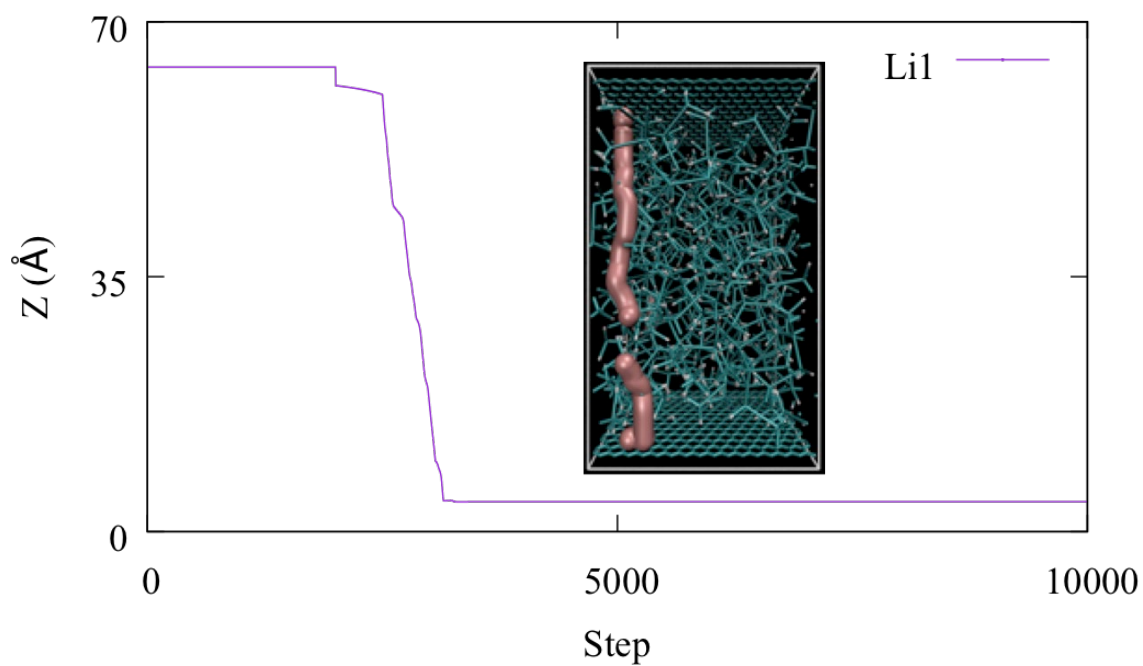
Figure 2. Plot of the z-axis active diffusion of lithium ion 1 through the OSPC-1 structure. Inset - trajectory of lithium ion 1 (pink) through the OSPC-1 structure (carbon –green, hydrogen – white) showing the charged graphene sheets at z = 70 Å (positive) and at z = 0 Å (negative).
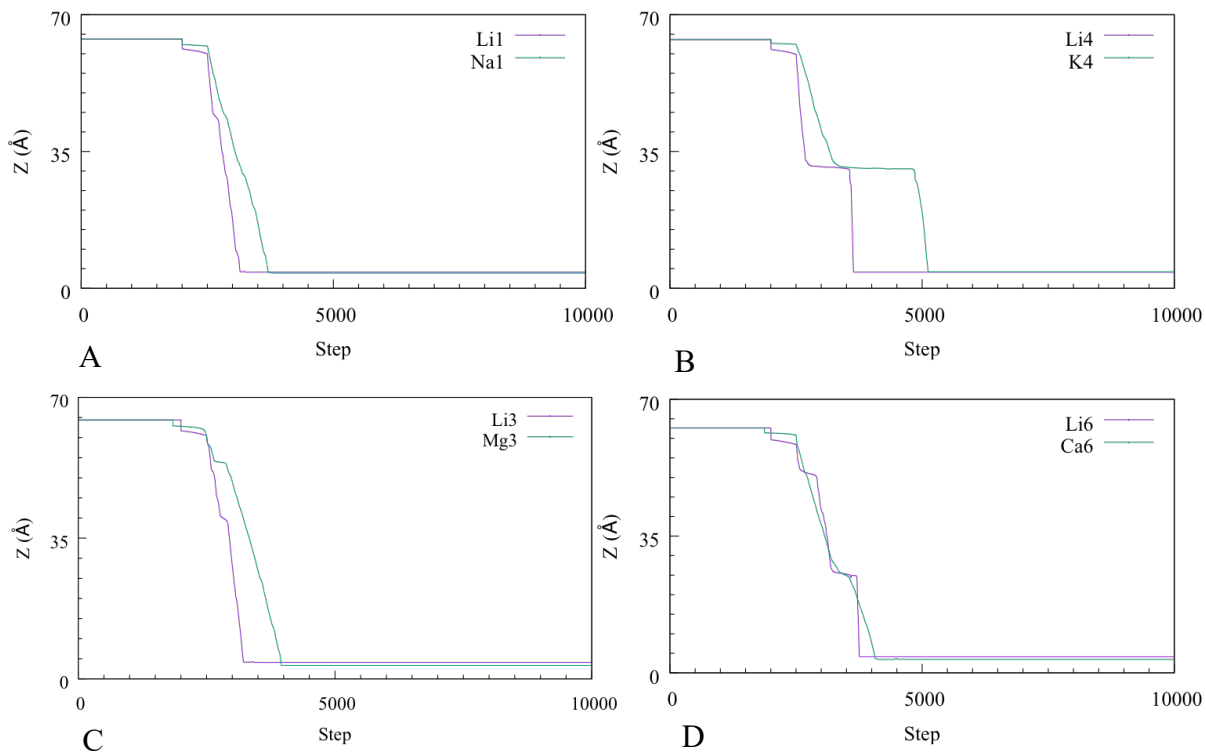
Figure 3. Plots of the z-axis active diffusion of ions through the OSPC-1 structure compared to the equivalent lithium ion. (a) Sodium ion 1, (b) Potassium ion 4, (c) Magnesium ion 3, and (d) Calcium ion 6.
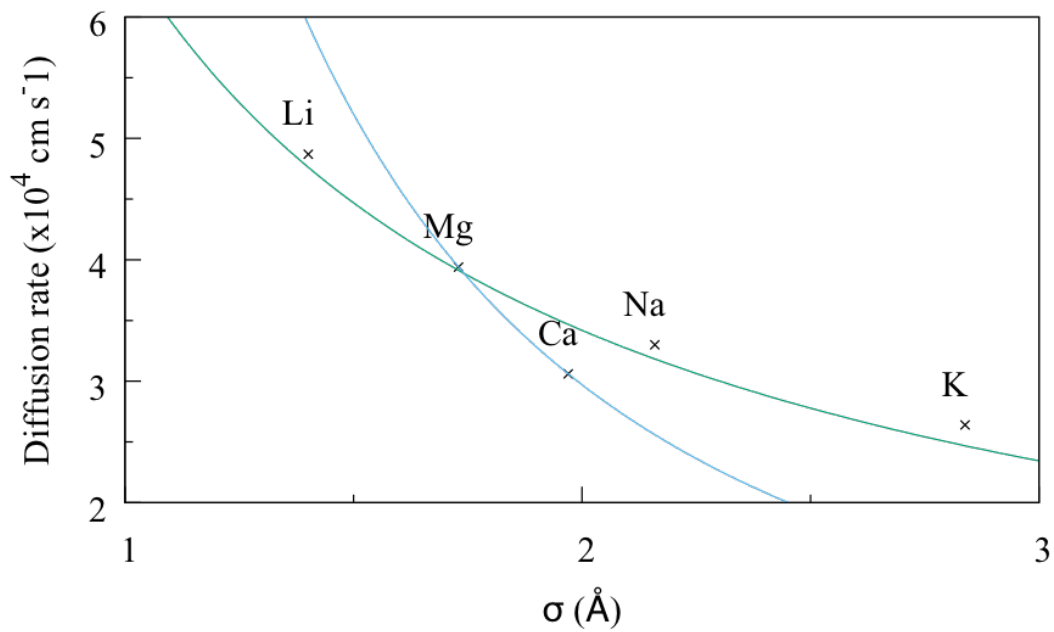
Figure 4. Plot of the average active diffusion rate of each ion against the σ value (ion radius) for each ion.
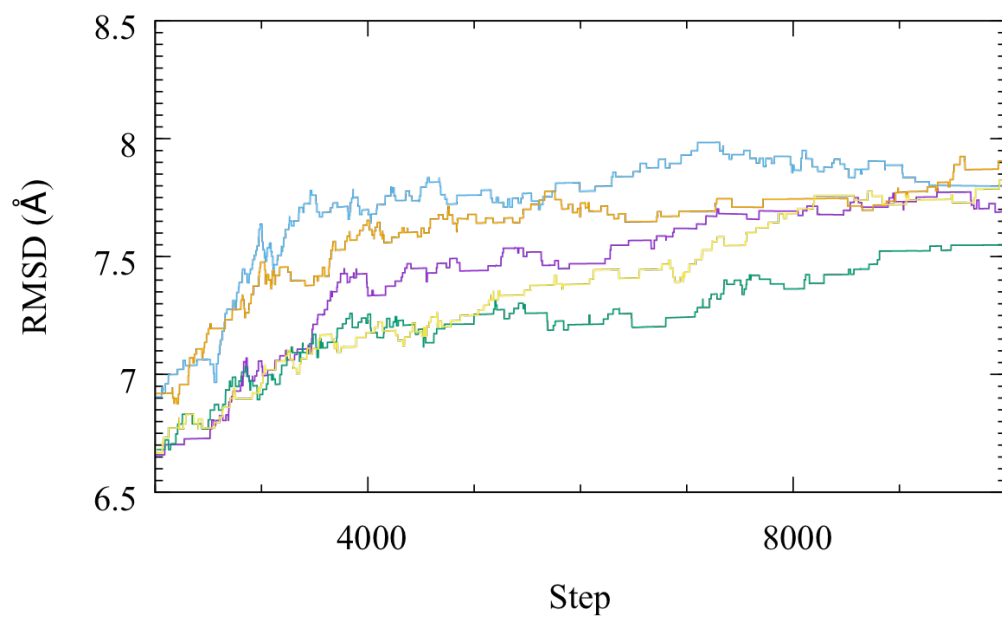
Figure 5. Plot of the root mean square displacement (RMSD) of the carbon atoms of the OSPC-1 structure. The RMSD is shown from the moment that the charges of the graphene sheet are activated. Lithium – pink, sodium – green, potassium – blue, magnesium – orange, and calcium – yellow.

Ion	σ (Å)	Capacity (mA h g^{-1})
Li	1.41	770
Na	2.16	386
K	2.83	158
Ca	1.97	774

Table 1. The average capacity for each ion in OSPC-1 calculated using Faradays's constant and the average uptake of each ion determined through simulated annealing.

Ion	Average active ion diffusion rate $(\text{x } 10^4 \text{ cm s}^{-1})$
Li	4.87
Na	3.30
K	2.64
Mg	3.94
Ca	3.06

Table 2. The average active diffusion rates calculated for each ion through OSPC-1.

References

1.   Kroto, H. W., Heath, J. R., O'Brien, S. C., Curl, R. F., and Smalley, R. E. C60: Buckminsterfullerene. *Nature,* **1985**, *318*, 162–163.

2.   Tarascon, J.-M., and Armand, M. Issues and Challenges Facing Rechargeable Lithium Batteries. *Nature*, **2001**, *414*, 359.

3.   Bruce, P. G., Scrosati, B. and Tarascon, J.-M. Nanomaterials for Rechargeable Lithium Batteries. *Angew. Chemie Int. Ed.,* **2008**, *47*, 2930–2946.

4.   Wang, H., Lu, Z., Qian, D., Li, Y., and Zhang, W. Single-crystal α-MnO_2 Nanorods: Synthesis and Electrochemical Properties. *Nanotechnology,* **2007,** *18*, 115616.

5.   Lin, Y.-M., Abel, P. R., Heller, A., and Mullins, C. B. α-Fe_2O_3 Nanorods as Anode Material for Lithium Ion Batteries. *J. Phys. Chem. Lett.,* **2011,** *2*, 2885–2891.

6.   Bai, Z., Fan, N., Sun, C., Ju, Z., Guo, C., Yang, J., and Qian, Y*.,* Facile Synthesis of Loaf-like $ZnMn_2O_4$ Nanorods and Their Excellent Performance in Li-ion Batteries. *Nanoscale,* **2013**, *5*, 2442–2447.

7.   Yang, T., Liu, Y., Huang, Z., Yang, Q., Guan, M., Fang, M., and Wu, X., A Facile Strategy for Fabricating Hierarchically Mesoporous Co_3O_4 Urchins and Bundles and Their Application in Li-ion Batteries with High Electrochemical Performance. *RSC Adv.,* **2015**, *5*, 24486–24493.

8.   Park, K., Cho, J., Jang, J., Yu, B., De La Hoz, A., Miller, K., Ellison, C., Goodenough, and J., Trapping, Lithium Polysulfides of a Li-S Battery by Forming Lithium Bonds in a Polymer Matrix. *Energy Environ. Sci.,* **2015***, 8,* 2389–2395.

9. Feng, Y., Yu, X.-Y., and Paik, U., Formation of Co_3O_4 Microframes from MOFs with Enhanced Electrochemical Performance for Lithium Storage and Water Oxidation. *Chem. Commun.,* **2016***, 52,* 6269–6272.

10. Bazilevsky, A. V, Yarin, A. L., and Megaridis, C. M., Co-electrospinning of Core-Shell Fibers Using a Single-Nozzle Technique. *Langmuir,* **2007***, 23*, 2311–2314.

11. Zhao, Z., Das, S., Xing, G., Fayon, P., Heasman, P., Jay, M., Bailey, S., Lambert, C., Yamada, H., Waikihara, T. Trewin, A., Ben, T., Qiu, S., and Valtchev, V., A 3D Organically Synthesized Porous Carbon Material for Lithium-Ion Batteries. *Angew. Chemie Int. Ed.,* **2018***, 57,* 11952–11956.

12. Eglinton, G. and Galbraith, A. R., Macrocyclic Acetylenic Compounds. Part I. Cyclotetradeca-1 :3-diyne and Related Compounds. *J. Chem. Soc.,* **1959,** 889–896.

13. Inc., A. S. Materials Studio 5.0.

14. Wessells, C. D., Peddada, S. V, Huggins, R. A., and Cui, Y., Nickel Hexacyanoferrate Nanoparticle Electrodes for Aqueous Sodium and Potassium Ion Batteries. *Nano Lett.,* **2011***, 11,* 5421–5425.

15. Slater, M. D., Kim, D., Lee, E., and Johnson, C. S., Sodium-Ion Batteries. *Adv. Funct. Mater.,* **2012***. 23*, 947–958.

16. Komaba, S., Hasegawa, T., Dahbi, M., and Kubota, K., Potassium Intercalation into Graphite to Realize High-Voltage/High-Power Potassium-ion Batteries and Potassium-ion Capacitors. *Electrochem. commun.,* **2015***, 60,* 172–175.

17. Gummow, R. J., Vamvounis, G., Kannan, M. B., and He, Y., Calcium-Ion Batteries: Current State-of-the-Art and Future Perspectives. *Adv. Mater.,* **2018***, 30,* 1801702.

18.   Ponrouch, A., Frontera, C., Bardé, F., and Palacin, M. R., Towards a Calcium-Based Rechargeable Battery. *Nat. Mater.,* **2015***, 15,* 169.

19.   Ponrouch, A. and Palacin, M. R., On the Road Toward Calcium-Based Batteries. *Curr. Opin. Electrochem.,* **2018***, 9,* 1–7.

20.   Singh, N., Arthur, T. S., Ling, C., Matsui, M. and Mizuno, F., A High Energy-Density Tin Anode for Rechargeable Magnesium-ion Batteries. *Chem. Commun.,* **2013***, 49,* 149–151.

21.   Yang, Z., Zhang, J., Kinter-Meyer, M., Lu, X., Choi, D., Lemmon, P., and Liu, J., Electrochemical Energy Storage for Green Grid. *Chem. Rev.,* **2011***, 111,* 3577–3613.

22.   Li, S., Qiu, J., Lai, C., Ling, M., Zhao, H., and Zhang, S., Surface Capacitive Contributions: Towards High Rate Anode Materials for Sodium Ion Batteries. *Nano Energy,* **2015***, 12,* 224–230.

23.   Fan, L. and Lu, B., Reactive Oxygen-Doped 3D Interdigital Carbonaceous Materials for Li and Na Ion Batteries. *Small,* **2016***, 12,* 2783–2791.

24.   Vadahanambi, S., Chun, H.-H., Jung, K. H., and Park, H., Nitrogen Doped Holey Carbon Nano-Sheets as Anodes in Sodium ion Battery. *RSC Adv.,* **2016***, 6,* 38112–38116.

25.   Xu, H., Gao, J. and Jiang, D., Stable, Crystalline, Porous, Covalent Organic Frameworks as a Platform for Chiral Organocatalysts. *Nat. Chem.,* **2015***, 7,* 905–912.

26.   Hou, H., Banks, C. E., Jing, M., Zhang, Y., and Ji, X., Carbon Quantum Dots and Their Derivative 3D Porous Carbon Frameworks for Sodium-Ion Batteries with Ultralong Cycle Life. *Adv. Mater.,* **2015***, 27,* 7861–7866.

27. Cao, B., Liu, H., Xu, B., Lei, Y., Chen, X., and Song, H., Mesoporous Soft Carbon as an Anode Material for Sodium Ion Batteries with Superior Rate and Cycling Performance. *J. Mater. Chem. A,* **2016***, 4,* 6472–6478.

28. Han, C., Han, K., Wang, X., Wang, C., Li, Q., Meng, J., Xu, X., He, Q., Luo, W., Wu, L., and Mai, L., Three-dimensional Carbon Network Confined Antimony Nanoparticle Anodes for High-capacity K-ion Batteries. *Nanoscale,* **2018***, 10,* 6820–6826.

29. Chen, Y., Luo, W., Carter, M., Zhou, L., Dai, J., Fu, K., Lacey, S., Li, T., Wan, J., Han, X., Bao, Y., and Hu, L., Organic Electrode for Non-aqueous Potassium-ion Batteries. *Nano Energy*, 2015, *18*, 205–211.

30. Lei, K., Li, F., Mu, C., Wang, J., Zhao, Q., Chen, C., and Chen, J., High K-storage Performance Based on the Synergy of Dipotassium Terephthalate and Ether-based Electrolytes. *Energy Environ. Sci.,* **2017***, 10,* 552–557.

31. Zhang, C., Qiao, Y., Xiong, P., Ma, W., Bai, P., Wang, X., Li, Q., Zhao, J., Xu, Y., Chen, Y., Zeng, J., Wang, F., Xu, Y., and Jiang, J., Conjugated Microporous Polymers with Tunable Electronic Structure for High-Performance Potassium-Ion Batteries. *ACS Nano,* **2019***, 13,* 745–754.

32. Jiang, J.-X., Trewin, A., Adams, D. J. and Cooper, A. I., Band Gap Engineering in Fluorescent Conjugated Microporous Polymers. *Chem. Sci.,* **2011***, 2,* 1777–1781.

33. Mass, R. C., Uchaker, E. and Cao, G., Beyond Li-ion: Electrode Materials for Sodium- and Magnesium-ion Batteries. *Sci. China Mater.,* **2015**, *58*, 715–766.

34. Lu, Z., Schechter, A., Moshkovich, M., and Aurbach, D., On the Electrochemical Behavior of Magnesium Electrodes in Polar Aprotic Electrolyte Solutions. *J. Electroanal. Chem.,* **1999***, 466,* 203–217.

35.   Novák, P., Imhof, R. and Haas, O. Magnesium Insertion Electrodes for Rechargeable Nonaqueous Batteries - a Competitive Alternative to Lithium? *Electrochim. Acta,* **1999**, 45, 351–367.

36.   Aurbach, D., Lu, Z., Schechter, A., Gofer, Y., Gizbar, H., Turgeman, R., Cohen, Y., Moshkovich, M., and Levi, E., Prototype Systems for Rechargeable Magnesium Batteries. *Nature,* **2000***, 407,* 724.

37.   Ichitsubo, T., Adachi, T., Yagi, S., and Doi, T., Potential Positive Electrodes for High-voltage Magnesium-ion Batteries. *J. Mater. Chem.,* **2011**, *21*, 11764–11772.

38.   Tian, H., Gao, T., Li, X., Wang, X., Luo, C., Fan, X., Yang, C., Suo, L., Ma, W., and Wang, C., High Power Rechargeable Magnesium/iodine Battery Chemistry. *Nat. Commun.,* **2017***, 8,* 14083.

39.   Zhao-Karger, Z., Gil Bardaji, M. E., Fuhr, O., and Fichtner, M. A New Class of Non-Corrosive, Highly Efficient Electrolytes for Rechargeable Magnesium Batteries. *J. Mater. Chem. A,* **2017**, *5*, 10815–10820.

40.   Aurbach, D., Skaletsky, R., and Gofer, Y. The Electrochemical Behaviour of Calcium Electrodes in a Few Organic Electrolytes. *J. Electrochem. Soc.,* **1991***, 138*, 3536–3545.

41.   Feng, X., Liu, L., Honsho, Y., Saeki, A., Seki, S., Irle, S., Dong, Y., Nagai, A., and Jiang, D., High-Rate Charge-Carrier Transport in Porphyrin Covalent Organic Frameworks: Switching from Hole to Electron to Ambipolar Conduction. *Angew. Chemie Int. Ed.,* **2012***, 51*, 2618–2622.

42.   Dauber-Osguthorpe, P., Roberts, V., Osguthorpe, D., Wolff, J., Genest, M., and Hagler, A*.,* Structure and Energetics of Ligand Binding to Proteins: Escherichia Coli

Dihydrofolate Reductase-Trimethoprim, a Drug-Receptor System. *Proteins Struct. Funct. Bioinforma.,* **1988***, 4,* 31–47.

43.   Maple, J. R., Dinur, U., and Hagler, A. T. Derivation of Force Fields for Molecular Mechanics and Dynamics from Ab Initio Energy Surfaces. *Proc. Natl. Acad. Sci.,* **1988***, 85,* 5350–5354.

44.   Hardy, B. J. and Sarko, A. Conformational Analysis and Molecular Dynamics Simulation of Cellobiose and Larger Cellooligomers. *J. Comput. Chem.,* **1993***, 14,* 831–847.

45.   Ritschl, F., Fait, M., Fiedler, K., Kohler, J., Kubias, B., and Meisei, M., An Extension of the Consistent Valence Force Field (CVFF) with the Aim to Simulate the Structures of Vanadium Phosphorus Oxides and the Adsorption of n-Butane and of 1-Butene on their Crystal Planes. *Zeitschrift für Anorg. und Allg. Chemie* **2002***, 628,* 1385–1396.

46.   Monti, D., Ponrouch, A., Araujo, R. B., Barde, F., Johansson, P., Palacín, M. R., Multivalent Batteries—Prospects for High Energy Density: Ca Batteries. *Frontiers in Chemistry,* **2019**, *7,* 79.

Table of Contents Graphic